THE JOURNAL OF PHYSICAL CHEMISTRY C

Article

pubs.acs.org/JPCC

Dynamic Jahn–Teller Effect in the Metastable High-Spin State of Solvated $[Fe(terpy)_2]^{2+}$

X. Zhang,[†] M. L. Lawson Daku,[‡] J. Zhang,[§] K. Suarez-Alcantara,[∥] G. Jennings,[†] C. A. Kurtz,[†] and S. E. Canton*[,∥]

[†]X-ray Sciences Division, Argonne, National Laboratory, 9700 South Cass Avenue, Argonne, Illinois 60439, United States

[‡]Département de Chimie Physique, Université de Genève, Quai E. Ansermet 30, CH-1211 Genève 4, Switzerland

[§]School of Environmental and Chemical Engineering, Tianjin Polytechnic University, Tianjin 300387, China

[∥]Department of Synchrotron Radiation Instrumentation, Lund University, P.O. Box 118, 22100 Lund, Sweden

Supporting Information

ABSTRACT: Characterizing structural distortions in the metastable spin states of d^4–d^7 transition metal ion complexes is crucial to understand the nature of their bistability and eventually control their switching dynamics. In particular, the impact of the Jahn–Teller effect needs to be assessed for any electronic configuration that could be effectively degenerate, as in e.g. the high-spin (HS) manifold of highly symmetric homoleptic Fe^{II} complexes. However, capturing its manifestations remains challenging since crystallization generally alters the molecular conformations and their interconversion. With the rapid progress of ultrafast X-ray absorption spectroscopy, it is now possible to collect data with unprecedented signal-to-noise ratio, opening up for detailed structural characterization of transient species in the homogeneous solution phase. By combining the analysis of picosecond X-ray absorption spectra with DFT simulations, the structure of the photoinduced HS state is elucidated for solvated $[Fe(terpy)_2]^{2+}$ (terpy = 2,2′:6′,2″-terpyridine). This species can be viewed as the average ^5B structure in D_2 symmetry that originates from a dynamic Jahn–Teller effect in the HS manifold. These results evidence the active role played by this particular instance of vibronic coupling in the formation of the HS state for this benchmark molecule. Ultimately, correlating the interplay between intramolecular and intermolecular degrees of freedom to conformational strain and distortions in real time should contribute to the development of advanced functionalities in transition metal ion complexes.

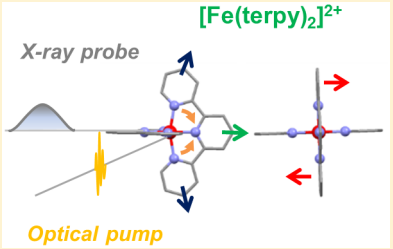

INTRODUCTION

Spin crossover (SCO) materials based on d^4–d^7 transition metal ion complexes are enabling novel strategies to perform sensing,[1−3] switching,[4−10] and information storage[11−16] in nanodevices. Tailoring the mesoscopic properties of these advanced materials for specific applications requires understanding the bistability displayed by their building blocks at the molecular level.[17−21] For the quasi-octahedral (O_h) $[Fe^{II}N_6]$ compounds, the ligand field (LF) splits the atomic-like 3d levels into t_{2g} and e_g orbitals. The relative strength of the LF splitting energy compared to the mean spin pairing energy determines the orbital populations and the energetics of the system.[22,23] A strong LF stabilizes the $(t_{2g})^6\ ^1A_{1g}$ low-spin (LS) state over the $(t_{2g})^4(e_g)^2\ ^5T_{2g}$ high-spin (HS) state, leading to an increase of the HS–LS zero-point energy difference ΔE_0.[22−24] The promotion of two electrons from the non- or weakly-bonding t_{2g} orbitals to the antibonding e_g orbitals causes an average elongation ΔR of all the metal–ligand (M–L) bonds.[22−24] The interdependence between ΔE_0 and ΔR is experimentally evidenced by the alterations in spin-state distributions that result from modifying the M–L bonds through e.g. chemical addition of bulky substituents,[25,26] encapsulation,[27,28] or applied external pressure.[29,30] The parameters ΔE_0 and ΔR also occur in the formulation of the HS → LS intersystem crossing as a nonadiabatic radiationless multiphonon process in the strong coupling limit.[31] When the HS population is impulsively triggered (e.g., photoinduced), the electronic and structural dynamics of the relaxation can be interpreted with kinetic models where ΔR, which identifies to the totally symmetric Fe–N breathing mode, enters as the single effective reaction coordinate.[32−35] The lifetime of the metastable HS state follows then the inverse energy gap law; i.e., it increases with decreasing ΔE_0.[32−35] Although a simple description of the static and dynamic properties in terms of ΔE_0 and ΔR explains numerous physicochemical trends, it is generally challenged whenever the structural changes undergone by the complex across the spin-state transition amount to significant anisotropic distortions of the first coordination sphere.[36−49] Among the phenomena leading to such deformations, the Jahn–Teller (JT) effect needs to be explicitly considered for any electronic configuration that could be effectively degenerate,[50,51] as in e.g. the HS manifold of highly symmetric homoleptic Fe^{II}

Received: November 23, 2014
Revised: December 23, 2014
Published: February 3, 2015

DOI: 10.1021/jp5117068
J. Phys. Chem. C 2015, 119, 3312−3321

complexes.[52,53] This distortion mediated by vibronic coupling enforces a symmetry lowering, which has a profound impact on the electronic and geometric structure of the HS state. As a mechanism for electron−phonon coupling, the JT effect promotes the synergy between the molecular attributes (e.g., optical and magnetic properties) and the response of the crystalline lattice during e.g. light-induced excited spin state trapping (LIESST) or cooperative phase transitions.[54−56] Connecting the characteristics of the JT distortion with the emergence of particular mesoscopic properties would allow manipulating this effect through chemical design in order to further develop the bottom-up multifunctionality of SCO materials.[52,53] A crucial step consists in describing the structural reorganization beyond an overall isotropic expansion of the metal coordination sphere. This in turn requires establishing the multimodal reaction coordinate that drives the anisotropic structural dynamics of the HS → LS transition. However, accessing the intrinsic JT distortion can seldom be achieved through crystallography because the molecular conformations are strongly perturbed by hydrogen bonding and packing forces.[57] As such, delineating the respective role of intra- and intermolecular factors in shaping a given structure is not straightforward. X-ray absorption spectroscopy (XAS) is a technique able to probe the local bonding environment around a specific element without relying on long-range order. Having reached the picosecond and femtosecond regimes,[58,59] this analytical tool has been successfully employed to track the photoinduced HS state of several $[Fe^{II}N_6]$ compounds solely affected by homogeneous solvation. An isotropic average bond elongation of $\Delta R \sim 0.2$ Å has been reported for $[Fe(bpy)_3]^{2+}$ (bpy = 2,2′-bipyridine),[60−65] $[Fe(phen)_3]^{2+}$ (phen = 1,10-phenanthroline),[66] and $[Fe(tren(py)_3]^{2+}$ (tren(py)$_3$ = tris(2-pyridin-2-ylmethanimino)ethyl)amine).[67−69] In the case of $[Fe(terpy)_2]^{2+}$, the possibility of extracting distinct ΔR for the two nonequivalent Fe−N bonds has been recently demonstrated, thus confirming that XAS is sensitive to the anisotropic distortion around the Fe center in the metastable HS state.[46] However, due to limited signal-to-noise (S/N) ratio, constraints had to be applied during the analysis of the photoinduced signal in order to restrict the number of variable parameters. A linear correlation inferred from the DFT optimization in D_{2d} symmetry was imposed between the two ΔR, and consequently, the manifestations of the JT effect have been eluding direct detection so far. Owing to the constant improvement of time-resolved XAS setups, the quality of the transient spectra is now rivaling the one delivered by static experiments, making it possible to retrieve detailed structural information without introducing any *a priori* constraints.[70] In the present work, the photoinduced HS state of solvated $[Fe(terpy)_2]^{2+}$(terpy = 2,2′:6′,2″-terpyridine) is reinvestigated with picosecond X-ray absorption spectroscopy (XAS). The excellent S/N ratio allows discriminating between the various predictions from density functional theory (DFT) optimization in D_{2d} and reduced D_2 symmetries. The comparison between experimental and theoretical results that take into account the symmetry lowering through vibronic coupling provides novel insights into the dynamical nature of the JT effect in the HS manifold for this benchmark complex.

MATERIALS AND METHODS

Synthesis. $[Fe(terpy)_2](PF_6)_2$[71] and the reference compound $[Fe(bpy)_3](PF_6)_2$[72] were prepared according to the published protocols. The commercial reagents were used without further purification.

Picosecond X-ray Absorption Spectroscopy. The time-resolved X-ray absorption spectroscopy (XAS) measurements were carried out at beamline 11ID-D of the APS, Argonne National Laboratory. The molecules were dissolved in acetonitrile (MeCN) to a 2 mM concentration. The solution was flown through a stainless steel tube forming a free jet of 550 μm in diameter. The sample was pumped with the second harmonic output of a Nd:YLF regenerative amplified laser at 527 nm (5 ps fwhm,1.6 kHz repetition rate). The diameter of the laser spot size was 0.6 mm at the sample position, yielding a fluence of 1 mJ/mm^2. The X-ray probe pulses were delivered by the APS storage ring during the 24-bunch operation mode, which is characterized by a 80 ps fwhm and a 6.5 MHz repetition rate. The X-ray spot size was 0.45 mm (horizontal) by 0.15 mm (vertical) at the sample position. Two avalanche photodiodes (APDs) positioned at a 90° angle on both sides of the incident X-ray beam collected the X-ray fluorescence signal. A soller slits/Mn filter combination, which was custom-designed for the specific sample chamber configuration and the corresponding sample−detector distance, was inserted between the jet and the APDs. The outputs of the APDs were sent to two fast analyzer cards (Agilent) that were triggered at the optical pump frequency by a signal from scattered laser light collected by a photodiode. The card digitized the X-ray fluorescence signal as a function of time at 1 ns/point after each trigger and averaged repeated measurements at a given integration time, typically 4 s. A third APD identical to the two sample detectors collected the X-ray photons from air scattering before the sample and was used as normalization signal. Every X-ray pulse between two laser triggers was recorded. The fluorescence signal from the synchronized X-ray pulse was collected at chosen time delay t after excitation by the optical pump pulse in order to construct the laser$_{ON}(t)$ trace. Each individual X-ray bunch between two laser pulses was divided by the signal from the normalization detector corresponding to the same bunch. The fluorescence signal from the same X-ray pulse was averaged over 20 round trips in the storage ring prior to the laser pulse in order to construct the laser$_{OFF}$ trace, which provided the spectrum of the ground state species μ_{GS}. The fitting of the difference signal $\Delta\mu(t) = [\text{laser}_{ON}(t) - \text{laser}_{OFF}]$ is described in the next section. The steady-state XAS spectrum of the reference powder sample was obtained in transmission mode at beamline I811 of the MAXlab swedish synchrotron facility.

XAS Data Analysis and Fitting Procedure. The analysis of the XAS data was performed with the Athena and Artemis programs interfaced to FEFF[73−75] and IFEFFIT.[76,77] Athena was used for pre-edge background removal, post-edge normalization, and atomic background subtraction. A R_{bkg} of 1 was chosen as upper limit of the low-R region. This parameter fixes the number of knots for the spline employed in the atomic background simulation through the equation

$$R_{knots} = \frac{2R_{bkg}\Delta k}{\pi}$$

Δk is the spline range in k space, where k is the photoelectron wavenumber defined as

$$k = \sqrt{\frac{2m(E - E_0)}{\hbar^2}}$$

DOI: 10.1021/jp5117068
J. Phys. Chem. C 2015, 119, 3312−3321

with E_0 being the absorption edge energy. The remaining oscillatory modulation $\chi(k)$ is due to constructive and destructive interferences between the wave of the outgoing photoelectron directly ionized from the core orbital and the wave of the photoelectron backscattered off the surrounding atoms. Therefore, the function $\chi(k)$ contains element-specific structural information. It can be expressed as

$$\chi(k) = \sum_i \frac{S_0^2 N_i f_i(k)}{kR_i^2} e^{-2k^2\sigma_i^2} e^{-2R_i/\lambda(k)} \sin[2kR_i + \delta_i(k)]$$

where $\lambda(k)$ is the photoelectron mean free path and S_0^2 is the amplitude reduction factor. For each neighboring shell i around the absorbing atom, $f_i(k)$ is the scattering amplitude, σ_i^2 is the Debye–Waller factor, R_i is the average distance of ith shell atom to the absorbing atom, and $\delta_i(k)$ is the corresponding phase shift. The DFT structure of the LS ground state was entered in Artemis in order to determine the scattering paths necessary to evaluate the $f_i(k)$. Figure 1 shows the geometric structure of $[Fe(terpy)_2]^{2+}$ and the atom labeling used in the EXAFS fitting procedure.

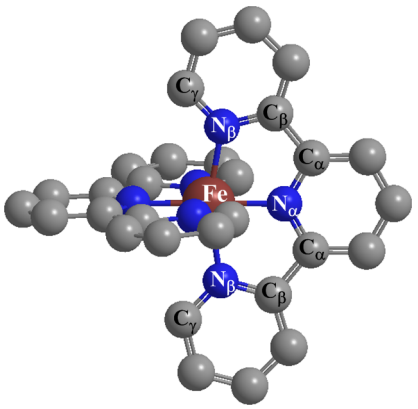

Figure 1. Schematic of the molecular structure of $[Fe(terpy)_2]^{2+}$ with the atom labeling used in the EXAFS fitting procedure.

The k range extended from 2 to 10.3 Å^{-1}. The contributions from all the paths in the first three scattering shells Fe–$N_{\alpha,\beta}$, Fe–$C_{\alpha,\beta,\gamma}$, and Fe–N–$C_{\alpha,\beta,\gamma}$ were included in the fitting procedure. For the ground state spectrum, each shell was assigned an R_i and a σ_i. All the paths shared a common S_0^2 and ΔE, which represents the amplitude reduction factor and the shift from the absorbing edge energy. The fraction of excited state population α needs to be estimated in order to extract the spectrum of the excited state $\mu_{ES}(t)$ from the difference trace $\Delta\mu(t)$. To that end, a set of excited state spectra was constructed based on the equation $\mu_{ES}(t) = (\Delta\mu(t)/\alpha) + \mu_{GS}$ with α varying from 0.7 to 0.95. They were then fitted while fixing the respective S_0^2, σ_i^2, and background to the ones obtained for the ground state. When using this suite of standard programs for XAS analysis, the fitting procedure is conducted within a reduced least-squares χ^2 framework that returns the R factor, the best-fit values for the chosen variables, and their error bars. The uncertainty on α was estimated from renormalizing the R factor as a function of α to 1, which allows taking this indicator as a conventional χ^2 estimate.[78] The value for which $\chi^2 = 2$ are the limits of the 1-σ confidence interval.

DFT Optimization. Density functional theory (DFT)[79,80] has been applied to the determination of the geometry adopted by the $[Fe(terpy)_2]^{2+}$ complex in the LS and in the HS state. The calculations have been performed with the ADF program package[81] using the PBE[82] and RPBE functional,[83] with the Slater-type TZP basis set of triple-ζ polarized quality from the ADF basis set database.[84,85] The calculations have been first performed for the complex in the gas phase. The influence of the acetonitrile solvent has then been taken into account using the conductor-like screening model (COSMO).[86−89]

RESULTS AND DISCUSSION

Photoinduced HS State of $[Fe(terpy)_2]^{2+}$ from Transient XAS Experiment. The ground state of $[Fe(terpy)_2]^{2+}$ corresponds to a $(t_{2g})^6$ LS configuration, for both the crystalline and the solution phase. The *mer*-tridentate coordination of the terpy ligand enforces a marked D_{2d} distortion of the first coordination sphere (FCS) away from ideal O_h symmetry, with the axial Fe–N_α bond length being shorter than the distal Fe–N_β one.[90−92] Upon pulsed laser excitation at λ_{exc} = 527 nm, a fraction α of the molecules is promoted to the HS state on the subpicosecond time scale.[46] Figure 2a shows the $\mu_{laser\_ON}(t)$

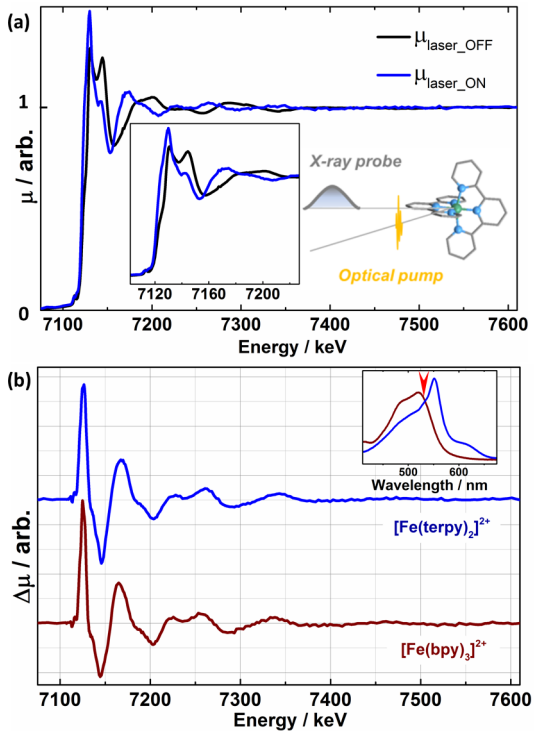

Figure 2. (a) μ_{laser_OFF} and $\mu_{laser\_ON}(t)$ traces at t = 120 ps for $[Fe(terpy)_2]^{2+}$. The inset zooms on the near-edge region. (b) Comparison between the difference traces $\Delta\mu(t) = [\mu_{laser\_ON}(t) - \mu_{laser\_OFF}]$ for $[Fe(terpy)_2]^{2+}$ (blue) and $[Fe(bpy)_3]^{2+}$ (red) at t = 120 ps. The inset shows the optical density for these two molecules. The red arrow indicates the excitation wavelength λ_{exc}.

(blue) and μ_{laser_OFF} (black) normalized XAS spectra at the Fe K-edge (E_0 = 7109 keV) for a pump–probe delay of t = 120 ps. The inset zooms on the near-edge region. The difference signal $\Delta\mu(t) = [\mu_{laser\_ON}(t) - \mu_{laser\_OFF}]$ is displayed in Figure 2b for $[Fe(terpy)_2]^{2+}$ (blue) and for $[Fe(bpy)_3]^{2+}$(red), which has been extensively studied with ultrafast X-ray techniques. The optical absorbance of the two species is given in the inset. The

DOI: 10.1021/jp5117068
J. Phys. Chem. C 2015, 119, 3312−3321

two $\Delta\mu(t)$ traces were obtained under the exact same experimental conditions (i.e., concentration, laser and X-ray focus, jet speed). The comparison with calibrated difference spectra of $[Fe(bpy)_3]^{2+}$[61−65] allows estimating an α of 80 ± 5% for this experiment. The modifications of the spectral line shapes in the near-edge region reflect the bond elongation in the FCS, common to all the HS states of $[Fe^{II}N_6]$ complexes.[60−69]

Figure 3a displays the k^2 weighted EXAFS function $\chi(k)$ extracted from μ_{laser_OFF} and $\mu_{laser\_ON}(t)$ spectra for the solvated

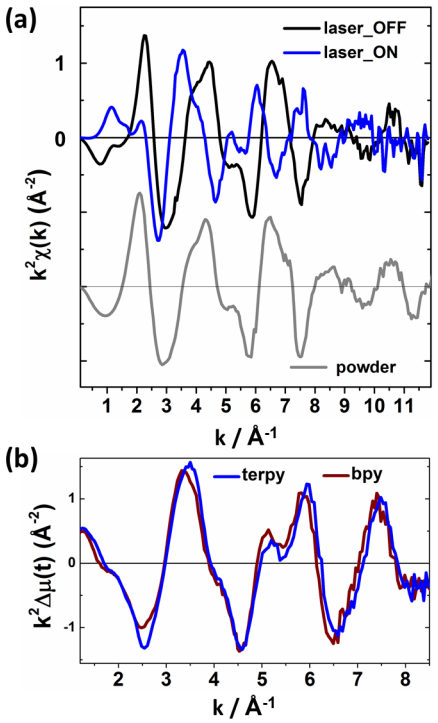

Figure 3. (a) EXAFS functions $k^2\chi(k)$ extracted from the μ_{laser_OFF} spectrum (black), from the μ_{laser_ON} (blue) traces, and from the μ spectrum a $[Fe(terpy)_2](PF_6)_2$ powder sample (gray). (b) EXAFS functions $k^2\chi(k)$ for μ_{laser_ON} of $[Fe(terpy)_2]^{2+}$ (blue) and $[Fe(bpy)_3]^{2+}$ (red).

$[Fe(terpy)_2]^{2+}$, along with the one obtained for a static XAS spectrum of solid $[Fe(terpy)_2](PF_6)_2$ (gray). It should be noted that the μ_{laser_OFF} spectrum is identical to the one of the powder sample, ruling out any influence of solvation on this profile. On a k scale, the slight alterations in oscillation amplitudes and the slow relative dephasing away from the edge energy can be traced back to the anisotropic expansion in $[Fe(terpy)_2]^{2+}$ over $[Fe(bpy)_3]^{2+}$ (Figure 3b).[46]

Figures 4a and 4b contain respectively the amplitude and the phase for the Fourier transform of $k^2\chi(k)$ in real (R) space directly extracted from the μ_{laser_OFF} and $\mu_{laser\_ON}(t)$ spectra. The fit parameters for the LS and HS states are summarized in Table 1. The value of 82 ± 8% obtained for α (Figure 4c) from the χ^2 minimization procedure is in excellent agreement with the reference measurements described above. Figure 4d shows the reconstructed $k^2\chi(k)$ of the corresponding excited state spectrum. The structural parameters obtained for the LS state are in accord with previous crystallographic measurements,[90−92] which report an average axial bond length Fe−N_α of 1.885 Å and an average distal bond length Fe−N_β of 1.981 Å. For the HS state, the bond lengths extracted from the XAS analysis can be compared to the results from DFT optimizations outlined in the next section.

Photoinduced HS State of $[Fe(terpy)_2]^{2+}$ from DFT Optimization. To date, modeling simultaneously the structures and the energetics of open-shell transition metal complexes with good accuracy remains theoretically challenging. In DFT, most modern exchange-correlation functionals adequately predict the geometry adopted by the complexes in the different spin states and the relative energies of the states within the spin manifolds. However, the results obtained for the energy difference between the states of different spin multiplicities strongly depend on the selected functional, and so far, no functional has emerged as the one of choice.[93−96] In this study, we have therefore used the PBE GGA functional, which exhibits the tendency of GGA functionals to strongly overestimate the HS−LS energy difference, along with the RPBE GGA functional, which was shown to give satisfactory estimates of this energy difference for $[Fe(bpy)_3]^{2+}$ and $[Fe(terpy)_2]^{2+}$.[42,93] The improved performance of RPBE over PBE was ascribed to its larger gradient exchange correction, and because correlation turns off relative to exchange with an increase of the latter,[97] RPBE tends to give slightly longer M−L bond than PBE.[93] Both functionals have been employed to optimize first the D_{2d} geometries of the LS and HS states for $[Fe(terpy)_2]^{2+}$ in the gas phase and in MeCN using the COSMO solvation model.[86−89] All the energetic and structural parameters are reported in the Supporting Information. In a LF of D_{2d} symmetry, the $^1A_{1g}$ (O_h) LS state becomes the $^1A_1$ (D_{2d}) state, while the $^5T_{2g}$ (O_h) HS state splits into the two tetragonal components ^5E (D_{2d}) and $^5B_2$ (D_{2d}). As expected, the values of the Fe−N bond lengths obtained with RPBE are systematically larger than with PBE (by about ∼0.03 Å) due to the enhanced exchange interaction. Considering first the LS state, passing from the gas phase to the solution phase mainly translates into a minor shortening of the Fe−N bonds, which can be viewed as a means of reducing the exposure of the ligand aromatic rings to the polar solvent. Overall, the solvated $^1A_1$ (D_{2d}) geometries of the LS species are in very good agreement with the reported crystallographic structures and the present XAS measurements. Considering then the HS state, the $^5B_2$ (D_{2d}) state is found to lie lower in energy than the ^5E (D_{2d}) state with both functionals. Inclusion of solvation effects leads to a slight decrease of the Fe−N distances and destabilizes the $^5B_2$ (D_{2d}) and ^5E (D_{2d}) with respect to $^1A_1$ (D_{2d}) state by about 700 cm^{-1}. Selected geometrical parameters for ^5E (D_{2d}) and $^5B_2$ (D_{2d}) are given in Table 2.

Comparison with the selected structural parameters returned by the present picosecond XAS analysis (Table 2) corroborates the earlier finding that the first coordination shell of the photoinduced HS state matches the one of the ^5E (D_{2d}) geometry better than the one of the $^5B_2$ (D_{2d}) geometry,[46] especially when considering the difference $R_{FE-N\alpha} - R_{Fe-N\beta}$ for which most of the systematic errors cancel out. However, such a result cannot be readily rationalized, since $^5B_2$ (D_{2d}) is actually the state of lowest energy. It should be pointed out that it is not possible to strictly conclude about the equilibrated HS geometry from the D_{2d} calculations due to vibronic instability. According to the JT theorem,[50,51] any nonlinear system presenting an electronic degeneracy is further distorted by the coupling to some specific molecular vibrations (i.e., the JT-active modes), so as to lower the symmetry and the total energy. Since the direct product $E \otimes E$ in D_{2d} contains the irreducible representations $A_1 + A_2 + B_1 + B_2$, the symmetries

DOI: 10.1021/jp5117068
J. Phys. Chem. C 2015, 119, 3312−3321

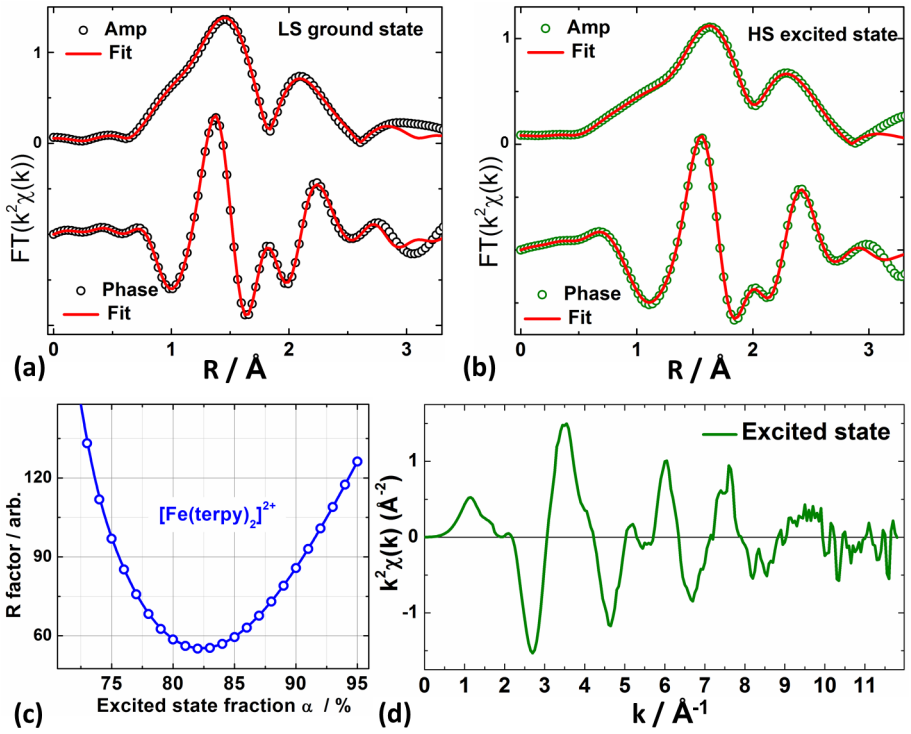

Figure 4. Amplitude and phase for the Fourier transform of the EXAFS function $k^2\chi(k)$ along with the best fit for (a) the LS ground state and for (b) the photoinduced HS state. (c) Fitted excited state fraction α. (d) The EXAFS function $k^2\chi(k)$ of the photoinduced HS state for $[Fe(terpy)_2]^{2+}$. The value for α employed to build the traces in (b) and (d) was 82%.

Table 1. Fit Parameters for the LS and HS States of Solvated $[Fe(terpy)_2]^{2+}$ [a]

	ΔE (eV)	S_0^2	R_{Fe-N_α} (Å) (D = 2)	R_{Fe-N_β} (Å) (D = 4)	$\sigma^2_{Fe-N_{\alpha,\beta}}$	R_{Fe-C_α} (Å) (D = 6)	R_{Fe-C_β} (Å) (D = 6)	R_{Fe-C_γ} (Å) (D = 6)	$\sigma^2_{Fe-C_{\alpha\beta\gamma}}$	$\sigma^2_{Fe-N_{\alpha\beta\text{-}\alpha\beta\gamma}}$	α (%)
LS	−1.9 ± 0.4	0.97 ± 0.1	1.86 ± 0.02	1.97 ± 0.02	0.003 ± 0.002	2.80 ± 0.03	2.83 ± 0.03	2.99 ± 0.03	0.004 ± 0.003	0.006 ± 0.004	
HS	0 ± 1	*0.97*	2.09 ± 0.02	2.18 ± 0.02	*0.003*	2.98 ± 0.02	3.02 ± 0.02	3.18 ± 0.02	*0.004*	*0.006*	82 ± 8

[a] D indicates the degeneracy of the scattering paths fixed in FEFF. The values kept constant during the optimization are indicated in italics.

Table 2. Comparison between Selected Structural Parameters in the HS State of Solvated $[Fe(terpy)_2]^{2+}$ Obtained from the Transient XAS Measurement and from the DFT Calculations in D_{2d} Symmetry (Ref 46 and This Work)

HS state	R_{Fe-N_α} (axial) (Å)	R_{Fe-N_β} (distal) (Å)	$R_{Fe-N_\alpha} - R_{Fe-N_\beta}$ (Å)	$R_{Fe-N_\alpha}/R_{Fe-N_\beta}$	R_{Fe-C_α} (Å) (D = 6)	R_{Fe-C_β} (Å) (D = 6)	R_{Fe-C_γ}(Å) (D = 6)
expt	2.09 ± 0.02	2.18 ± 0.02	0.09 ± 0.04	0.96 ± 0.04	2.98 ± 0.03	3.02 ± 0.03	3.18 ± 0.03
RPBE/TZP results							
complex solvated in MeCN							
DFT (^{5}E)-MeCN-D_{2d}	2.124	2.218	0.094	0.958	3.036	3.070	3.193
DFT ($^5B_2$)-MeCN-D_{2d}	2.180	2.212	0.032	0.986	3.081	3.092	3.166
PBE/TZP results							
complex solvated in MeCN							
DFT (^{5}E)-MeCN-D_{2d}	2.095	2.188	0.093	0.957	3.005	3.037	3.161
DFT ($^5B_2$)-MeCN D_{2d}	2.148	2.179	0.031	0.986	3.046	3.056	3.132

of the non-totally symetric JT-active modes for the ^{5}E (D_{2d}) state are a_2, b_1, and b_2. The $^5B_2$ (D_{2d}) geometry also exhibits a vibrational instability, which is characterized by the presence of e modes with imaginary frequencies of large modules. This probably arises from the vibronic coupling between the $^5B_2$ (D_{2d}) state and the close-lying ^{5}E (D_{2d}) state. In order to account for these effects, the optimizations were undertaken in the reduced D_2 symmetry. Upon $D_{2d} \rightarrow D_2$ symmetry lowering, $^5B_2$ (D_{2d}) becomes $^5B_1$ (D_2) while ^{5}E (D_{2d}) splits into $^5B_2$ (D_2) and $^5B_3$ (D_2), these two extrema of the HS potential energy surface being equivalent when interchanging the x- and y-axes. As expected, the JT effect has an impact on the ^{5}E (D_{2d}) configuration. Both in the gas phase and in MeCN, the $^5B_2$ (D_2) and $^5B_3$ (D_2) states are now predicted with PBE and the RPBE to be quasi-degenerate with $^5B_1$ (D_2) within the so-called chemical accuracy of ±350 cm^{-1} (see Supporting Information). The $^5B_1$ (D_2) state is predicted to coincide with the $^5B_2$ (D_{2d}) state on the HS potential energy surface. Attempting to localize it invariably returns either the ^5B (D_{2d}) state or the $^5B_1$ (D_2)

DOI: 10.1021/jp5117068
J. Phys. Chem. C 2015, 119, 3312−3321

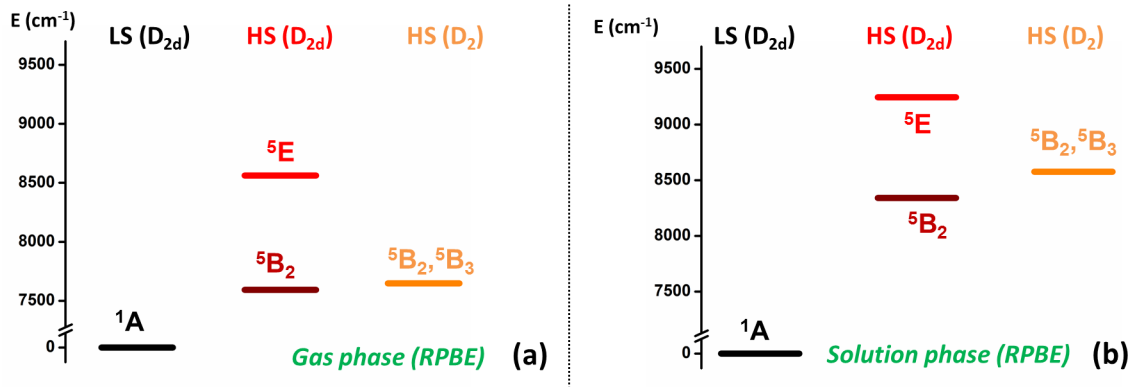

Figure 5. Sketch summarizing the energies of the LS and HS manifols in D_{2d} and D_2 symmetries obtained with the RPBE functional for $[Fe(terpy)_2]^{2+}$ in the gas phase and in MeCN.

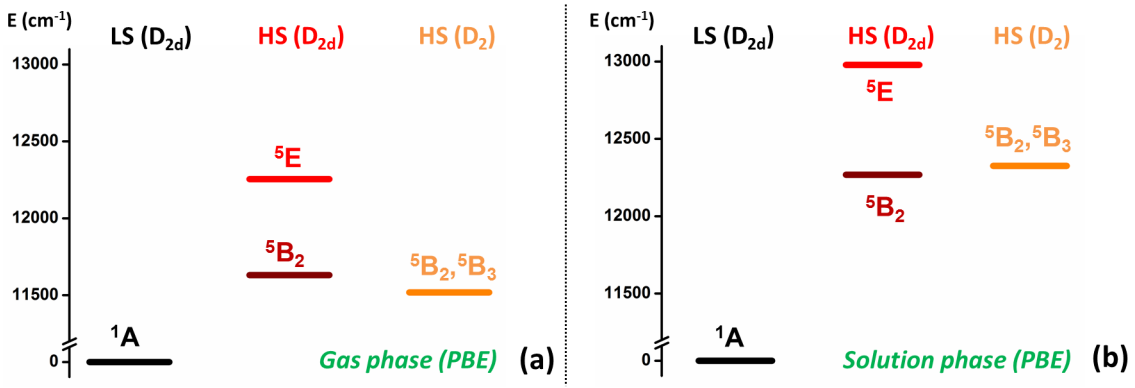

Figure 6. Sketch summarizing the energies of the LS and HS manifols in D_{2d} and D_2 symmetries obtained with the PBE functional for $[Fe(terpy)_2]^{2+}$ in the gas phase and in MeCN.

Table 3. Comparison between Selected Structural Parameters in the HS State of Solvated $[Fe(terpy)_2]^{2+}$ Obtained from the Transient XAS Measurement and from the DFT Calculations in D_2 Symmetry

HS state	R_{Fe-N_α} (axial) (Å)	R_{Fe-N_β} (distal) (Å)	$R_{Fe-N_\alpha} - R_{Fe-N_\beta}$ (Å)	$R_{Fe-N_\alpha}/R_{Fe-N_\beta}$	R_{Fe-C_α} (Å) (D = 6)	R_{Fe-C_β} (Å) (D = 6)	R_{Fe-C_γ} (Å) (D = 6)
expt	2.09 ± 0.02	2.18 ± 0.02	0.09 ± 0.04	0.96 ± 0.04	2.98 ± 0.03	3.02 ± 0.03	3.18 ± 0.03
RPBE/TZP results							
complex solvated in MeCN DFT ($^5B_2$,$^5B_3$))-MeCN-D_2	2.127	2.224	0.097	0.956	3.040	3.075	3.203
PBE/TZP results							
complex solvated in MeCN DFT ($^5B_2$,$^5B_3$))-MeCN-D_2	2.100	2.189	0.089	0.960	3.008	3.040	3.160

component of the excited ligand-field ^5E (O_h) state originating from the $(t_{2g})^3(e_g)^3$ (O_h) configuration. The calculations performed in the gas phase and in MeCN led to a D_2 $^5B_2$ geometry, which is given as a minimum by the vibrational analysis conducted on the gas-phase geometry. The energetics of the complex in the gas phase and solvated in MeCN for the D_{2d} and D_2 symmetries are displayed in Figures 5 and 6. The comparison with the selected structural parameters returned by the present picosecond XAS analysis is outlined in Table 3. Finally, it should be noted that the geometries optimized in the lower C_2 symmetry systematically resemble very closely the ones obtained in D_2 symmetry. This can be readily traced back to the fact that the various HS states only differ through the occupation of the split t_{2g} nonbonding orbitals.

Dynamic Nature of the Vibronic Coupling in the Photoinduced HS State of $[Fe(terpy)_2]^{2+}$. The present experimental and theoretical results clearly demonstrate that including the JT effect is crucial for obtaining a consistent picture of the electronic and geometric structure adopted by the solvated HS state. Since the electron−phonon coupling strength is always finite in solution phase, the fluctuations due to the ionic motions have to be considered in order to understand the dynamic nature of the vibronic coupling across the spin-state transition. Several studies have already suggested that the solvent plays a significant role. For example, the crystal structure of $[Fe(terpy)_2(ClO_4)_2]H_2O$,[90] where the complex is in the LS state, reveals that some solvent molecules are nested in the accessible voids between the ligands, reflecting a strong conformational correlation of the complex with its first solvation shell. Upon photoabsorption, the Franck−Condon state is formed instantaneously in the average solvent cage that was accommodating the LS ground state. It then decays via ultrafast intersystem crossing to the HS state, in which the high-frequency Fe−N stretching mode and some of the low-

DOI: 10.1021/jp5117068
J. Phys. Chem. C 2015, 119, 3312−3321

frequency modes involving ligands and solvent are collectively excited. Whenever the electronic configuration would be degenerate, the JT-active modes also take part to the stabilization of the equilibrated HS state, as reported here for the photoinduced HS state of $[Fe(terpy)_2]^{2+}$ in MeCN. Concurrently, the solvent molecules reorient around the vibrationally hot HS state as it thermalizes within a few picoseconds by dissipating the excess energy to the surroundings as heat. Overall, the structural changes in the first solvation shell amount to more than 50% of the bulk solvent reorganization energy for $[Fe(terpy)_2]^{2+}$ in dimethyl sulfoxide.[98] Femtosecond transient absorption spectroscopy in the UV−vis region has also shown that the unimolecular rate constants of the HS → LS transition are solvent-dependent for most $[Fe^{II}N_6]$ complexes.[99−101] These findings highlight the necessity of developing further the multiscale description of spin-state transitions. Theoretically, a full vibronic treatment beyond the Born−Oppenheimer approximation has to be performed considering that the internal electronic and the nuclear degrees of freedom are all strongly coupled.[102−105] In addition, the solvation models have to be refined in order to account for the specific solute−solvent interactions.[102−106] Experimentally, establishing the multimodal reaction coordinate of the spin-state transition requires tracking the ultrafast structural dynamics with spin and element sensitivity on several length scales scale. Although an exhaustive real-time mapping at the molecular level is still currently lacking, the essential tools are rapidly emerging, and some of them have already been applied to the benchmark complex $[Fe(bpy)_3]^{2+}$ in aqueous solution. Femtosecond X-ray emission spectroscopy measurements have recently uncovered the intermediate triplet state that mediates the photoinduced formation of its HS state.[107] Simultaneous X-ray spectroscopy and scattering experiments reaching the typical ∼100 ps temporal resolution at a storage ring facility have captured the global structural changes in the photoexcited solute, the temperature increase in the bulk solvent, and the density increase associated with the response of the caging solvent.[65] This last observation quantitatively agrees with *ab initio* molecular dynamics (MD) simulations predicting that the Fe−N bond elongation in the HS state triggers on average the expulsion of two water molecules from the first solvation shell.[102] An improved model electronic Hamiltonian[104,105] has been employed in the MD simulations of the low-lying electronic states of $[Fe(bpy)_3]^{2+}$ in aqueous solution. For this complex, the $^5T_{2g}$ (O_h) HS state is split by the D_3 LF into the ^5E (D_3) and $^5A_1$ (D_3) components. Under the influence of the JT effect, ^5E (D_3) further splits into the $^5A_2$ (C_2) and ^5B (C_2) states, while $^5A_1$ (D_3) becomes the $^5A_1$ (C_2) state. These MD simulations indicate that the ^5B (C_2) component is stabilized compared to ^5E (D_3) but that the $^5A_1$ (C_2) remains the state of lowest energy, a conclusion, which could be readily tested with picosecond XAS measurements achieving high S/N ratio. Comparing the manifestations of the dynamic JT effect for the bidentate and tridentate coordination in Fe^{II} complexes also awaits similar *ab initio* MD simulations and complementary ultrafast X-ray scattering measurements for the HS state of solvated $[Fe(terpy)_2]^{2+}$.

CONCLUSION

In summary, the transient HS state of solvated $[Fe(terpy)_2]^{2+}$ has been reinvestigated through the analysis of picosecond X-ray spectra obtained with high S/N ratio. The comparison with DFT calculations performed in D_{2d} and D_2 symmetry shows that this species can be viewed as the average ^5B structure in D_2 symmetry that originates from a dynamic Jahn−Teller effect in the HS manifold. These results highlight the importance of accounting for this effect in order to conciliate the energetics and the structural parameters obtained through experiment and theory. More generally, this study suggests that intramolecular vibronic coupling, which is strongly influenced by specific interactions with the solvation shell, plays a crucial role in the formation of the metastable state. Consequently, establishing the complete reaction coordinate that encodes the ultrafast structural dynamics of spin-state transitions in 3d transition metal complexes requires elaborating a refined atomic-scale description for the interplay between intramolecular and intermolecular degrees of freedom. Harnessing the detailed characterization of subtle structural rearrangements should facilitate the tailoring of the anisotropic distortions within this class of complexes in order to tune their electronic and magnetic properties. Since investigations in the homogeneous solution phase are accessing intrinsic deformations, they constitute stepping stones in the design of novel strategies able to translate molecular distortion and conformational strain into advanced functionalities.

ASSOCIATED CONTENT

Supporting Information

Results of the optimization calculations performed for $[Fe(terpy)_2]^{2+}$ in the gas phase and in acetonitrile. This material is available free of charge via the Internet at http://pubs.acs.org.

AUTHOR INFORMATION

Corresponding Author

*E-mail sophie.canton@desy.de (S.E.C.).

Present Address

K.S.-A.: Unidad Morelia del Instituto de Investigaciones en Materiales, Universidad Nacional Autónoma de México, Antigua Carretera a Pátzcuaro No. 8701, Col. Ex Hacienda de San José de la Huerta, C.P. 58190, Morelia, Michoacán, México.

Notes

The authors declare no competing financial interest.

ACKNOWLEDGMENTS

The Swedish Research Council and the Crafoord Foundation are greatly acknowledged as funding sources. X.Z., G.J., C.A.K., and the use of the Advanced Photon Source were supported by the U.S. Department of Energy, Office of Science, Office of Basic Energy Sciences, under Contract DE-AC02-06CH11357. The theoretical work was supported by allocations of computing time from the Swiss National Supercomputing Centre (CSCS) under project IDs s103 and s296 and the Center for Advanced Modeling Science (CADMOS) under project ID CTESIM. We thank Pr L. X. Chen (Argonne National Laboratory and Northwestern University) for initial contributions on the Nd:YLF laser. Finally, we thank Pr. A. Hauser, Pr. S. Iuchi, and Dr Y. Liu for helpful comments and stimulating discussions.

REFERENCES

(1) Southon, P. D.; Liu, L.; Fellows, E. A.; Price, D. J.; Halder, G. J.; Chapman, K. W.; Moubaraki, B.; Murray, K. S.; Letard, J.-F.; Kepert, C. J. Dynamic Interplay between Spin-Crossover and Host-Guest

DOI: 10.1021/jp5117068
J. Phys. Chem. C 2015, 119, 3312−3321

Function in a Nanoporous Metal-Organic Framework Material. *J. Am. Chem. Soc.* **2009**, *131*, 10998−11009.
(2) McHale, R.; Liu, Y. B.; Ghasdian, N.; Hondow, N. S.; Ye, S. J.; Lu, Y.; Brydson, R.; Wang, X. S. Dual Lanthanide Role in the Designed Synthesis of Hollow Metal Coordination (Prussian Blue Analogue) Nanocages with Large Internal Cavities and Mesoporous Cage. *Nanoscale* **2011**, *3*, 3685.
(3) Bao, X.; Sheperd, H. J.; Salmon, L.; Molnar, G.; Tong, M. L.; Bousseksou, A. The Effect of an Active Guest on the Spin Crossover Phenomenon. *Angew. Chem., Int. Ed.* **2013**, *52*, 1198−1202.
(4) Gütlich, P.; Garcia, Y.; Woike, T. Photoswitchable Coordination Compounds. *Coord. Chem. Rev.* **2001**, *219*−*221*, 839−879.
(5) Diefenbach, M.; Kim, K. S. Toward Molecular Magnetic Switches with an Electrical Bias. *Angew. Chem., Int. Ed.* **2007**, *46*, 7640−7643.
(6) Lorenc, M.; Hebert, J.; Moisan, N.; Trzop, E.; Servol, M.; Buron-Le Cointe, M.; Cailleau, H.; Boillot, M. L.; Pontecorvo, E.; Wulff, M.; et al. Successive Dynamical Steps of Photoinduced Switching of a Molecular Fe(III) Spin-Crossover Material by Time-Resolved X-Ray Diffraction. *Phys. Rev. Lett.* **2009**, *103*, 028301.
(7) Bertoni, R.; Lorenc, M.; Tissot, A.; Servol, M.; Boillot, M. L.; Collet, E. Femtosecond Spin-State Photoswitching of Molecular Nanocrystals Evidenced by Optical Spectroscopy. *Angew. Chem., Int. Ed.* **2012**, *51*, 7485−7489.
(8) Abdul-Kader, K.; Lopes, M.; Bartual-Murgui, C.; Kraieva, O.; Hernandez, E. M.; Salmon, L.; Nicolazzi, W.; Carcenac, F.; Thibault, C.; Molnar, G.; Bousseksou, A. Synergistic Switching of Plasmonic Resonances and Molecular Spin States. *Nanoscale* **2013**, *5*, 5288−5293.
(9) Schneider, B.; Demeshko, S.; Dechert, S.; Meyer, F. A. Double-Switching Multistable Fe-4 Grid Complex with Stepwise Spin-Crossover and Redox Transitions. *Angew. Chem., Int. Ed.* **2010**, *49*, 9274−9277.
(10) Matsumoto, T.; Newton, G. N.; Shiga, T.; Hayami, S.; Matsui, Y.; Okamoto, H.; Kumai, R.; Murakami, Y.; Oshio, H. Programmable Spin-State Switching in a Mixed-Valence Spin-Crossover Iron Grid. *Nat. Commun.* **2014**, *5*, 4865.
(11) Kahn, O.; Martinez, C. J. Spin-Transition Polymers: From Molecular Materials Toward Memory Devices. *Science* **1998**, *279*, 44−48.
(12) Boillot, M. L.; Zarembovitch, J.; Sour, A. Ligand-Driven Light-Induced Spin Change (LD-LISC): a Promising Photo Magnetic Effect. *Top. Curr. Chem.* **2004**, *234*, 261−276.
(13) Feng, X.; Mathonière, C.; Jeon, I.-R.; Rouzières, M.; Ozarowski, A.; Aubrey, M. L.; Gonzalez, M. I.; Clérac, R.; Long, J. R. Tristability in a Light-Actuated Single-Molecule Magnet. *J. Am. Chem. Soc.* **2013**, *135*, 15880−15884.
(14) Cavallini, M.; Bergenti, I.; Milita, S.; Ruani, G.; Salitros, I.; Qu, Z.-R.; Chandrasekar, R.; Ruben, M. Micro- and Nanopatterning of Spin-Transition Compounds into Logical Structures. *Angew. Chem., Int. Ed.* **2008**, *47*, 8596−8600.
(15) Hao, H.; Zheng, X. H.; Song, L. L.; Wang, R. N.; Zeng, Z. Electrostatic Spin Crossover in a Molecular Junction of a Single-Molecule Magnet Fe-2. *Phys. Rev. Lett.* **2012**, *108*, 017202.
(16) Baadji, N.; Piacenza, M.; Tugsuz, T.; Della Sala, F.; Maruccio, G.; Sanvito, S. Electrostatic Spin Crossover Effect in Polar Magnetic Molecules. *Nat. Mater.* **2009**, *8*, 813−817.
(17) Létard, J.-F.; Guinneau, P.; Goux-Capes, L. Towards Spin Crossover Applications. *Top. Curr. Chem.* **2004**, *235*, 221−249.
(18) Bousseksou, A.; Molnár, G.; Salmon, L.; Nicolazzi, W. Molecular Spin Crossover Phenomenon: Recent Achievements and Prospects. *Chem. Soc. Rev.* **2011**, *40*, 3313−3335.
(19) Halcrow, M. A. Structure:Function Relationships in Molecular Spin-Crossover Complexes. *Chem. Soc. Rev.* **2011**, *40*, 4119−4142.
(20) Murray, K. S. The Development of Spin-Crossover Research. In *Spin-Crossover Materials: Properties and Applications*; Halcrow, M. A., Ed.; John Wiley & Sons Ltd.: Oxford, UK, 2013; doi 10.1002/9781118519301.ch1.
(21) Gaspar, A. B.; Seredyuk, M. Spin Crossover in Soft Matter. *Coord. Chem. Rev.* **2014**, *268*, 41−58.
(22) Gütlich, P.; Goodwin, H. A. Spin Crossover - An Overall Perspective. *Top. Curr. Chem.* **2004**, *233*, 1−47.
(23) Hauser, A. Ligand Field Theoretical Considerations. *Top. Curr. Chem.* **2004**, *233*, 49−58.
(24) Goodwin, H. A. Spin Crossover in Iron(II) Tris(diimine) and Bis(terimine) Systems. *Top. Curr. Chem.* **2004**, *233*, 59−90.
(25) Wang, Y.-T.; Li, S.-T.; Wu, S.-Q.; Cui, A.-L.; Shen, D.-Z.; Kou, H.-Z. Spin Transitions in Fe(II) Metallogrids Modulated by Substituents, Counteranions, and Solvents. *J. Am. Chem. Soc.* **2013**, *135*, 5942−5945.
(26) Hamon, P.; Tpot, J.-Y.; Le Floch, M.; Boulon, M.-E.; Cador, O.; Golhen, S.; Ouahab, L.; Fadel, L.; Saillard, J.-Y.; Hamon, J.-R. Dramatic Remote Substitutent Effects on the Electronic Spin State of Bis(scorpionate) Iron(II) Complexes. *Angew. Chem., Int. Ed.* **2008**, *47*, 8687−8691.
(27) Ono, K.; Yoshlzawa, M.; Aklta, M.; Kato, T.; Tsunobuchl, Y.; Ohkoshi, S.-I.; Fujita, M. Spin Crossover by Encapsulation. *J. Am. Chem. Soc.* **2009**, *131*, 2782−2783.
(28) Halder, G. J.; Kepert, C. J.; Moubaraki, B.; Murray, K. S.; Cashion, J. D. Guest-Dependent Spin Crossover in a Nanoporous Molecular Framework Material. *Science* **2002**, *298*, 1762−1765.
(29) Grey, J. K.; Butler, I. S. Effects of High External Pressures on the Electronic Spectra of Coordination Compounds. *Coord. Chem. Rev.* **2001**, *219*−*221*, 713−759.
(30) Gütlich, P.; Ksenofontov, V.; Gaspar, A. B. Pressure Effect Studies on Spin Crossover Systems. *Coord. Chem. Rev.* **2005**, *249*, 1811−1829.
(31) Buhks, E.; Navon, G.; Bixon, M.; Jortner, J. Spin Conversion Processes in Solutions. *J. Am. Chem. Soc.* **1980**, *102*, 2918−2923.
(32) Hauser, A. Intersystem Crossing in the $[Fe(ptz)_6](BF_4)_2$ Spin Crossover System (ptz = 1-Propyltetrazole). *J. Chem. Phys.* **1991**, *94*, 2741−2748.
(33) Hauser, A.; Vef, A.; Adler, P. Intersystem Crossing dynamics in Fe(II) Coordination Compounds. *J. Chem. Phys.* **1991**, *95*, 8710−8717.
(34) Hinek, R.; Spiering, H.; Schollmeyer, D.; Gutlich, P.; Hauser, A. The $[Fe(etz)_6](BF_4)_2$ Spin-crossover System - Part One: High-Spin ⇆ Low-Spin Transition in Two Lattice Sites. *Angew. Chem., Int. Ed.* **1996**, *35*, 1427−1434.
(35) Hauser, A. Light-Induced Spin Crossover and the High-Spin → Low-Spin Relaxation. *Top. Curr. Chem.* **2004**, *234*, 155−198.
(36) Renz, F.; Oshio, H.; Ksenofontov, V.; Waldeck, M.; Spiering, H.; Gütlich, P. Strong Field Iron(II) Complex Converted by Light Into a Long-Lived High-Spin State. *Angew. Chem., Int. Ed.* **2000**, *39*, 3699−3700.
(37) Oshio, H.; Spiering, H.; Ksenofontov, V.; Renz, F.; Gütlich, P. Electronic Relaxation Phenomena Following Co-57(EC)Fe-57 Nuclear Decay in $[Mn\text{-}II(terpy)_2](ClO_4)_2$ (1)/$2H_2O$ and in the Spin Crossover Complexes $[Co\text{-}II(terpy)_2]X\text{-}2\ nH_2O$ (X = Cl and ClO_4): A Mossbauer Emission Spectroscopic Study. *Inorg. Chem.* **2001**, *40*, 1143−1150.
(38) Marchivie, M.; Guionneau, P.; Létard, J.-P.; Chasseau, D. Towards Direct Correlations Between Spin-Crossover and Structural Features in Iron(II) Complexes. *Acta Crystallogr., Sect. B* **2003**, *59*, 479−486.
(39) Alvarez, S. Relationships Between Temperature, Magnetic Moment, and Continuous Symmetry Measures in Spin Crossover Complexes. *J. Am. Chem. Soc.* **2003**, *125*, 6795−6802.
(40) Marchivie, M.; Guionneau, P.; Létard, J.-F.; Chasseau, D. Photoinduced Spin-Transitions: the Role of the Iron(II) Environment Distortion. *Acta Crystallogr., Sect. B* **2005**, *61*, 25−28.
(41) Nakamura, M. Electronic Structures of Highly Deformed Iron(III) Porphyrin Complexes. *Coord. Chem. Rev.* **2006**, *250*, 2271−2294.
(42) Hauser, A.; Enachescu, C.; Lawson-Daku, M. L.; Vargas, A.; Amstutz, N. Low-Temperature Lifetimes of Metastable High-Spin States in Spin-Crossover and in Low-Spin Iron(II) Compounds: The Rule and Exceptions to the Rule. *Coord. Chem. Rev.* **2006**, *250*, 1642−1652.

DOI: 10.1021/jp5117068
J. Phys. Chem. C 2015, 119, 3312−3321

(43) Legrand, V.; Pillet, S.; Weber, H.-P.; Souhassou, M.; Letard, J.-F.; Guionneau, P.; Lecomte, C. On the Precision and Accuracy of Structural Analysis of Light-Induced Metastable States. *J. Appl. Crystallogr.* **2007**, *40*, 1076−1088.
(44) Bernien, M.; Wiedemann, D.; Hermanns, C. F.; Krueger, A.; Rolf, D.; Kroener, W.; Mueller, P.; Grohmann, A.; Kuch, W. Spin Crossover in a Vacuum-Deposited Submonolayer of a Molecular Iron(II) Complex. *J. Phys. Chem. Lett.* **2012**, *3*, 3431−3434.
(45) Hou, J.; Wang, Q.; Sun, Q.; Kawazoe, Y.; Jena, P. J. Strain-Induced Spin Crossover in Phtalocyanine-Based Organometallic Sheets. *J. Phys. Chem. Lett.* **2012**, *3*, 3109−3114.
(46) Canton, S. E.; Zhang, X.; Lawson Daku, L. M.; Smeigh, A. L.; Zhang, J.; Liu, Y.; Wallentin, C.-J.; Attenkofer, K.; Jennings, G.; Kurtz, C. A.; et al. Probing the Anisotropic Distortion of Photoexcited Spin Crossover Complexes with Picosecond X-ray Absorption Spectroscopy. *J. Phys. Chem. C* **2014**, *118*, 4536−4545.
(47) Cho, H.; Strader, M. L.; Hong, K.; Jamula, L.; Gullikson, E. M.; Kim, T. K.; deGroot, F. M. F.; McCusker, J. K.; Schoenlein, R. W.; Huse, N. Ligand-Field Symmetry Effects in Fe(II) Polypyridyl Compounds Probed by Transient X-ray Absorption Spectroscopy. *Faraday Discuss.* **2012**, *157*, 463−474.
(48) Bowman, D. N.; Jakubikova, E. Low-Spin versus High-Spin Ground State in Pseudo-Octahedral Iron Complexes. *Inorg. Chem.* **2012**, *51*, 6011−6019.
(49) Papai, M.; Vanko, G.; de Graaf, C.; Rozgonyi, T. Theoretical Investigation of the Electronic Structure of Fe(II) Complexes at Spin-State Transitions. *J. Chem. Theory Comput.* **2013**, *9*, 509−519.
(50) Bersuker, I. B. The Concept of Vibronic Interactions in Crystal Sterochemistry of Transition Metal Compounds. *J. Coord. Chem.* **1995**, *34*, 289.
(51) Köppel, Y.; Köppel, H.; Yarkony, D. R.; Barentzen, H. The Jahn Teller Effect: Fundamentals and Implications for Physics and Chemistry. *Springer Ser. Chem. Phys.* **2009**, *87*, 915.
(52) Halcrow, M. A. Iron(II) Complexes of 2,6-Di(pyrazol-1-yl)pyridines-A Versatile System for Spin-Crossover Research. *Coord. Chem. Rev.* **2009**, *253*, 2493−251.
(53) Halcrow, M. A. Jahn-Teller Distortions in Transition Metal Compounds, and Their Importance in Functional Molecular and Inorganic Materials. *Chem. Soc. Rev.* **2013**, *42*, 1784−1795.
(54) Tayagaki, T.; Tanaka, K. Photoinduced Phase Transition to a New Macroscopic Spin-Crossover-Complex Phase. *Phys. Rev. Lett.* **2001**, *86*, 2886−2889.
(55) Tokoro, H.; Ohkoshi, S. Photo-Induced Phase Transition in RbMnFe Prussian Blue Analog-Based Magnet. *Springer Ser. Opt. Sci.* **2010**, *155*, 1−35.
(56) Enachescu, C.; Nishino, M.; Miyashita, S. Theoretical Descriptions of Spin-Transitions in Bulk Lattices. In *Spin-Crossover Materials: Properties and Applications*; Halcrow, M. A., Ed.; John Wiley & Sons Ltd.: Oxford, UK, 2013; doi 10.1002/9781118519301.ch18.
(57) Tao, J.; Wei, R.-J.; Huang, R.-B.; Zheng, L.-S. Polymorphism in Spin-Crossover Systems. *Chem. Soc. Rev.* **2012**, *41*, 703−737.
(58) Chergui, M. () Ultrafast Studies of the Light-Induced Spin Change in Fe(II)-Polypyridine Complexes. In *Spin-Crossover Materials: Properties and Applications*; Halcrow, M. A., Ed.; John Wiley & Sons Ltd.: Oxford, UK, 2013; doi 10.1002/9781118519301.ch15.
(59) Chen, L. X.; Zhang, X. Photochemical Processes Revealed by X-ray Transient Absorption Spectroscopy. *J. Phys. Chem. Lett.* **2013**, *4*, 4000−4013.
(60) Gawelda, W.; Pham, V. T.; Benfatto, M.; Zaushitsyn, Y.; Kaiser, M.; Grolimund, D.; Johnson, S. L.; Abela, R.; Hauser, A.; Bressler, C.; et al. Structural Determination of a Short-Lived Excited Iron(II) Complex by Picosecond X-ray Absorption Spectroscopy. *Phys. Rev. Lett.* **2007**, *98*, 057401.
(61) Bressler, C.; Milne, C.; Pham, V.-T.; ElNahhas, A.; van der Veen, R. M.; Gawelda, W.; Johnson, S.; Beaud, P.; Grolimund, D.; Kaiser, M.; et al. Femtosecond XANES Study of the Light-Induced Spin Crossover Dynamics in an Iron(II) Complex. *Science* **2009**, *323*, 489−492.
(62) Cannizzo, A.; Milne, C. J.; Consani, C.; Gawelda, W.; Bressler, C.; van Mourik, F.; Chergui, M. Light-Induced Spin Crossover in Fe(II)-Based Complexes: The Full Photocycle Unraveled by Ultrafast Optical and X-ray Spectroscopies. *Coord. Chem. Rev.* **2010**, *254*, 2677−2686.
(63) Lemke, H. T.; Bressler, C.; Chen, L. X.; Fritz, D. M.; Gaffney, K. J.; Galler, A.; Gawelda, W.; Haldrup, K.; Hartsock, R. W.; Ihee, H.; et al. Femtosecond X-ray Absorption Spectroscopy at a Hard X-ray Free Electron Laser: Application to Spin Crossover Dynamics. *J. Phys. Chem. A* **2013**, *117*, 735−740.
(64) Lima, F. A.; Milne, C. J.; Amarasinghe, D. C. V.; Rittmann-Franck, M. H.; van der Veen, R. M.; Reinhard, M.; Pham, V. T.; Karlsson, S.; Johnson, S. L.; Grolimund, D.; et al. A High-Repetition Rate Scheme for Synchrotron-Based Picosecond Laser Pump/X-ray Probe Experiments on Chemical and Biological Systems in Solution. *Rev. Sci. Instrum.* **2011**, *82*, 063111.
(65) Haldrup, K.; Vanko, G.; Gawelda, W.; Galler, A.; Doumy, G.; March, A. M.; Kanter, E.; Bordage, A.; Dohn, A.; van Driel, T. B.; et al. Guest-Host Interactions Investigated by Time-Resolved X-ray Spectroscopies and Scattering at MHz Rates: Solvation Dynamics and Photoinduced Spin Transition in Aqueous $Fe(bipy)_3^{2+}$. *J. Phys. Chem. A* **2012**, *116*, 9878−9887.
(66) Nozawa, S.; Sato, T.; Chollet, M.; Ichiyanagi, K.; Tomita, A.; Fujii, H.; Adachi, S.; Koshihara, S. Direct Probing of Spin State Dynamics Coupled with Electronic and Structural Modifications by Picosecond Time-Resolved XAFS. *J. Am. Chem. Soc.* **2010**, *132*, 61−63.
(67) Khalil, M.; Marcus, M. A.; Smeigh, A. L.; McCusker, J. K.; Chong, H. H. W.; Schoenlein, R. W. Picosecond X-ray Absorption Spectroscopy of a Photoinduced Iron(II) Spin Crossover Reaction in Solution. *J. Phys. Chem. A* **2006**, *110*, 38−44.
(68) Huse, N.; Kim, T. K.; Jamula, L.; McCusker, J. K.; deGroot, F. M. F.; Schoenlein, R. W. Photo-Induced Spin-State Conversion in Solvated Transition Metal Complexes Probed via Time-Resolved Soft X-ray Spectroscopy. *J. Am. Chem. Soc.* **2010**, *132*, 6809−6816.
(69) Huse, N.; Cho, H.; Hong, K.; Jamula, L.; deGroot, F. M. F.; Kim, T. K.; McCusker, J. K.; Schoenlein, R. W. Femtosecond Soft X-ray Spectroscopy of Solvated Transition-Metal Complexes: Deciphering the Interplay of Electronic and Structural Dynamics. *J. Phys. Chem. Lett.* **2011**, *2*, 880−884.
(70) Zhang, X.; Canton, S. E.; Smolentsev, G.; Wallentin, C.-J.; Liu, Y.; Kong, Q.; Attenkofer, K.; Stickrath, A. B.; Mara, M. W.; Chen, L. X.; Wärnmark, K.; Sundström, V. Highly Accurate Excited-State Structure of $[Os(bpy)_2dcbpy]^{2+}$ Determined by X-ray Transient Absorption Spectroscopy. *J. Am. Chem. Soc.* **2014**, *136*, 8804−8809.
(71) Hathcock, D. J.; Stone, K.; Madden, J.; Slattery, S. J. Electron Substituent Effects on Reddox and Spin State Properties of Iron(II) Bis-Terpyridyl Complexes. *Inorg. Chim. Acta* **1998**, *282*, 131−135.
(72) Bouzaid, J.; Schultz, M.; Lao, Z.; Bartley, J.; Bostrom, T.; McMurtrie, J. Supramolecular Selection in Molecular Alloy. *Cryst. Growth Des.* **2012**, *12*, 3906−3916.
(73) http://leonardo.phys.washington.edu/feff.
(74) Ravel, B.; Newville, M. J. ATHENA, ARTEMIS, HEPHAESTUS: Data Analysis for X-ray Absorption Spectroscopy Using IFEFFIT. *J. Synchrotron Radiat.* **2005**, *12*, 537−541.
(75) http://cars9.uchicago.edu/ifeffit/.
(76) Ankudinov, A. L.; Ravel, B.; Rehr, J. J.; Conradson, S. D. Real-Space Multiple-Scattering Calculation and Interpretation of X-ray-Absorption Near-Edge Structure. *Phys. Rev. B* **1998**, *58*, 7565−7576.
(77) Newville, M. IFEFFIT: Interactive XAFS Analysis and FEFF Fitting. *J. Synchrotron Radiat.* **2001**, *8*, 322−324.
(78) Jun, S.; Lee, J. H.; Kim, J.; Kim, J.; Kim, K. H.; Kong, Q. Y.; Kim, T. K.; Lo Russo, M.; Wulff, M.; Ihee, H. Photochemistry of $HgBr_2$ in Methanol Investigated Using Time-Resolved X-ray Liquidography. *Phys. Chem. Chem. Phys.* **2010**, *12*, 11536−11547.
(79) Hohenberg, P.; Kohn, W. Inhomogeneous Electron Gas. *Phys. Rev.* **1964**, *136*, B864.
(80) Kohn, W.; Sham, L. J. Self-Consistent Equations Including Exchange and Correlation Effects. *Phys. Rev.* **1965**, *140*, A1133.

DOI: 10.1021/jp5117068
J. Phys. Chem. C 2015, 119, 3312−3321

(81) te Velde, G.; Bickelhaupt, F. M.; Baerends, E. J.; Fonseca Guerra, C.; van Gisbergen, S. J. A.; Snijders, J. G.; Ziegler, T. Chemistry with ADF. *J. Comput. Chem.* **2001**, *22*, 931−967.
(82) Perdew, J. P.; Burke, K.; Ernzerhof, M. Generalized Gradient Approximation Made Simple. *Phys. Rev. Lett.* **1996**, *77*, 3865.
(83) Hammer, B.; Hansen, L. B.; Nørskov, J. K. Improved Adsorption Energetics within Density-Functional Theory Using Revised Perdew-Burke-Ernzerhof Functionals. *Phys. Rev. B* **1999**, *59*, 7413−7421.
(84) Chong, D. P. Completeness Profiles of One-Electron Basis Sets. *Can. J. Chem.* **1995**, *73*, 79−83.
(85) Van Lenthe, E.; Baerends, E. J. Optimized Slater-Type Basis Sets for the Elements 1−118. *J. Comput. Chem.* **2003**, *24*, 1142−1156.
(86) Klamt, A. Conductor-like Screening Model for Real Solvents: A New Approach to the Quantitative Calculation of Solvation Phenomena. *J. Chem. Phys.* **1995**, *99*, 2224−2235.
(87) Klamt, A.; Jonas, V. Treatment of the Outlying Charge in Continuum Solvation Models. *J. Chem. Phys.* **1996**, *105*, 9972−9981.
(88) Klamt, A.; Schüürmann, G. COSMO: A New Approach to Dielectric Screening in Solvents with Explicit Expressions for the Screening Energy and its Gradient. *J. Chem. Soc., Perkin Trans. 2* **1993**, 799−805.
(89) Pye, C. C. Ziegler, An Implementation of the Conductor-Like Screening Model of Solvation within the Amsterdam Density Functional Package. *Theor. Chem. Acc.* **1999**, *101*, 396−408.
(90) Baker, A. T.; Goodwin, H. A. Crystal-Structure of Bis(2,2′-6′,2″-terpyridine)iron(II) Bis(perchlorate) Hydrate. *Aust. J. Chem.* **1985**, *38*, 207−214.
(91) Laine, P.; Gourdon, C. A.; Launay, J.-P. Chemistry of Iron with Dipicolinic Acid. 4. Mixed-Ligand Complexes of Iron(III) and Related Compounds. *Inorg. Chem.* **1995**, *34*, 5156−5165.
(92) McMurtrie, J.; Dance, I. Engineering Grids of Metal Complexes: Development of the 2D $M(terpy)_2$ Embrace Motif in Crystals. *CrystEngComm* **2005**, *7*, 216−229.
(93) Lawson Daku, L. M.; Vargas, A.; Hauser, A.; Fouqueau, A.; Casida, M. E. Assessment of Density Functionals for the High-Spin/Low-Spin Energy Difference in the Low-Spin Iron(II) Tris(2,2′-bipyridine) Complex. *ChemPhysChem* **2005**, *6*, 1393−1410.
(94) Keep, K. P. Consistent Descriptions of Metal−ligand Bonds and Spin-Crossover in Inorganic Chemistry. *Coord. Chem. Rev.* **2013**, *257*, 196−209.
(95) Paulsen, H.; Schänemann, V.; Wolny, J. A. Progress in Electronic Structure Calculations on Spin-Crossover Complexes. *Eur. J. Inorg. Chem.* **2013**, *2013*, 628−641.
(96) Lawson Daku, L. M. Modeling Transition Metal Complexes in the Framework of the Spin-Crossover Phenomenon: A DFT Perspective. *Curr. Inorg. Chem.* **2013**, *3*, 242−259.
(97) Perdew, J. P.; Kurth, S. *Lect. Notes Phys.* **2003**, *620*, 1.
(98) Spence, T. G.; Trotter, B. T.; Posey, L. A. Influence of Sequential Solvation on Metal-to-Ligand Charge Transfer in Bis-(2,2′,2″-terpyridyl)iron(II) Clustered with Dimethyl Sulfoxide. *J. Phys. Chem. A* **1998**, *102*, 7779−7786.
(99) Creutz, C.; Chou, M.; Netzel, T. L.; Okumura, M.; Sutin, N. Lifetimes, Spectra, and Quenching of the Excited-States of Polypyridine Complexes of Iron(II), Ruthenium(II), and Osmium(II). *J. Am. Chem. Soc.* **1980**, *102*, 1309−1319.
(100) McCusker, J. K.; Walda, K. N.; Dunn, R. C.; Simon, J. D.; Magde, D.; Hendrickson, D. N. Subpicosecond. $^1MLCT \rightarrow {}^5T_2$ Instersystem Crossing of Low-Spin Polypyridyl Ferrous Complexes. *J. Am. Chem. Soc.* **1993**, *115*, 298−307.
(101) Tribollet, J.; Galle, G.; Jonusauskas, G.; Deldicque, D.; Tondusson, M.; Letard, J.-F.; Freysz, E. Transient Absorption Spectroscopy of the Iron(II) $[Fe(phen)_3]^{2+}$ Complex: Study of the Non-Radiative Relaxation of an Isolated Iron(II) Complex. *Chem. Phys. Lett.* **2011**, *513*, 42−47.
(102) Lawson-Daku, M. L.; Hauser, A. Ab Initio Molecular Dynamics Study of an Aqueous Solution of $[Fe(bpy)_3](Cl)_2$ in the Low-Spin and in the High-Spin States. *J. Phys. Chem. Lett.* **2010**, *1*, 1830−1835.
(103) Swart, M.; Güel, M.; Solà, M. A Multi-scale Approach to Spin Crossover in Fe(II) Compounds. *Phys. Chem. Chem. Phys.* **2011**, *13*, 10449−10456.
(104) Iuchi, S. A Model Electronic Hamiltonian to Study Low-Lying Electronic States of $[Fe(bpy)_3]^{2+}$ in Aqueous Solution. *J. Chem. Phys.* **2012**, *136*, 064519.
(105) Iuchi, S.; Koga, N. An Improved Model Electronic Hamiltonian for Potential Energy Surfaces and Spin-Orbit Couplings of Low-Lying d-d States of $[Fe(bpy)_3]^{2+}$. *J. Chem. Phys.* **2014**, *140*, 024309.
(106) Nalbach, P.; Achner, A. J. A.; Frey, M.; Grosser, M.; Bressler, C.; Thorwart, M. Hydration Shell Effects in the Relaxation Dynamics of Photoexcited Fe-II Complexes in Water. *J. Chem. Phys.* **2014**, *14*, 044304.
(107) Zhang, W.; Alonso-Mori, R.; Bergmann, U.; Bressler, C.; Chollet, M.; Galler, A.; Gawelda, W.; Hadt, R. G.; Hartsock, R. W.; Kroll, T.; et al. Tracking Excited-State Charge and Spin Dynamics in Iron Coordination Complexes. *Nature* **2014**, *509*, 345−348.

DOI: 10.1021/jp5117068
J. Phys. Chem. C 2015, 119, 3312−3321